Accurate Event-Driven Motion Compensation Incorporating All Detected Events

A. Rahmim, K. Dinelle, J. C. Cheng, M. A. Shilov, W. P. Segars, O. G. Rousset, B. M. W. Tsui, D. F. Wong, V. Sossi

***Abstract*— This work develops and investigates a formalism for accurate motion-compensated reconstruction, including elaborate consideration of scattered and random coincidences, which at the same time is particularly feasible in the context of high-resolution PET. The method takes into consideration normally-detected projection data which are not detected due to motion. Furthermore, it incorporates information from *all* detected events, particularly those which, following correction for motion, fall outside the FoV (e.g. axially or through detector gaps), thus satisfying a mathematical requirement, elaborated in the text, that would allow accurate motion averaging of sensitivity factors in *image-space* (as opposed to projection-space). The proposed method has been extensively validated using phantom experiments as well as realistic simulations of a new mathematical brain phantom developed in this work.**

I. Introduction

With continuous improvements in spatial resolution of PET scanners, small patient movements during PET imaging become a significant source of resolution degradation. An ongoing trend consists of using external accurate tracking of motion (as opposed to merely relying on the emission data for the motion estimation task). In this context, a number of reconstruction approaches have been suggested:

(1) Use of multiple acquisition frames (MAFs) [1] which are individually reconstructed, motion-compensated and summed: the major limitation of the MAF approach is that lowering the motion threshold can result in the acquisition of many *low-statistic* frames.

(2) Post-processing of the motion-blurred reconstructed images using de-convolution operators [3]. This method, however, has not attracted much attention because it amplifies the noise in the PET data.

3) Another method [4] models motion blurring in the forward-projection step of the EM algorithm, so as to ensure better matching of the estimated image and the measured, motion-blurred data. This is, however, an *ad hoc* approach and can exhibit severe non-convergence [8].

A. Rahmim, O. G. Rousset and D. F. Wong are with the Division of Nuclear Medicine, Department of Radiology, Johns Hopkins University, Baltimore MD 21205 (e-mail arahmim1@jhmi.edu, pvcorrection@yahoo.com, dfwong@jhmi.edu).

K. Dinelle, J. C. Cheng and V. Sossi are with the Department of Physics and Astronomy, University of British Columbia, Vancouver BC V6T 1Z1 (e-mail kdinelle@phas.ubc.ca, jcheng@phas.ubc.ca, vesna@phas.ubc.ca).

M. A. Shilov, W. P. Segars and B. M. W. Tsui are with Division of Med. Imaging Physics, Depart.of Radiology, Johns Hopkins University, Baltimore MD 21205 (e-mail mshilov1@jhmi.edu, wsegars1@jhmi.edu, btsui1@jhmi.edu).

Alternatively, a more comprehensive approach involves system matrix modeling of the motion information (thus applied in both the forward and back-projection steps, as well as in the sensitivity image), as proposed for rigid motion [8], and respiratory non-gated [5] as well as respiratory/cardiac gated data [6], [7], though the latter does not involve motion-contaminated data (as the data are gated, thus different motion modeling is used for each gate).

(4) Correcting individual lines-of-response (LORs) for motion [9]. This approach (in its purely event-driven form) may result in reconstructed image artifacts (e.g. see [11]). In this work, we propose a comprehensive scheme, *including* corrections for randoms and scattered events, that seeks to eliminate shortcomings of the purely event-driven approach, and at the same time is very practical to implement.

II. Beyond the Purely Event-Driven Approach

The purely event-driven approach neglects two issues [11], which we shall refer to as *issue-1* and *issue-2*:

(*Issue-1*) An LOR that is in the field-of-view (FoV) can fall outside the FoV because of motion. This therefore results in a loss of events that would normally have been detected.

(*Issue-2*) On the other hand, an event that is normally not detected, i.e. is not in the field-of-view (FoV), may fall within the FoV because of motion. Therefore, after correction for motion, some detected events may correspond to no actual detector pairs.

These two effects can occur both in the axial and transaxial directions, as depicted in Fig. 1.

Neglecting *issue-1* can produce image artifacts, as demonstrated by simulation [10], [12], [13] or experimentally [11]. On the other hand, neglecting *issue-2*, as commonly done in the literature, (i) can result in a loss of signal-to-noise ratio (SNR) in the images (for instance, even small amounts of motion result in substantial interaction with detector gaps which in the HRRT scanner occupy nearly 10% of the entire sinogram-space); furthermore (ii) as elaborated shortly, consideration of these additional events can be shown to yield a very useful mathematical property resulting in a *very considerable* (e.g. by a factor of $\sim$30 for the HRRT scanner) reduction in the computational task of calculating the sensitivity correction factors in the EM algorithm.

In the next section, an accurate (yet very practical) approach addressing both of the aforementioned issues, with particular

1-4244-0561-0/06/$20.00 ©2006 IEEE.

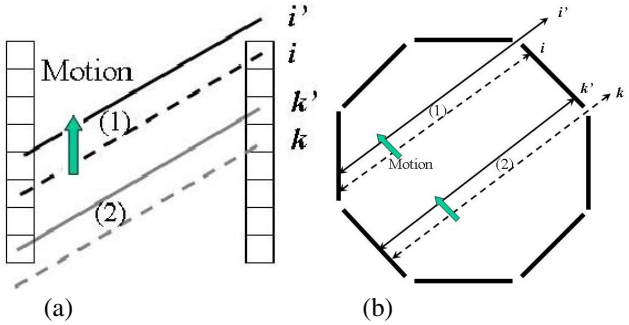

Fig. 1. (a) Axial motion can result in (*issue-1*): a detectable LOR i to fall outside the FoV (shown as i'), and can also result in (*issue-2*): an out-of-FoV LOR k to fall within the FoV (shown as k'). (b) Transaxial motion, for scanners with gaps in between the detector heads, can result in the exact same issues as shown in (a). The effects are shown due to translation, but are equally valid for rotation.

attention to corrections for randoms and scattered events in the presence of motion, is elaborated.

III. Accurate Motion Correction including Correction for Randoms and Scattered Events

A. Histogram-mode EM Reconstruction

Denoting f_j^m as the activity (i.e. emission *rate*) in voxel j (j=1...J) estimated at the m^{th} iteration, and p_{ij} as the probability of an emission from voxel j being detected along LOR i, the ordinary Poisson expectation maximization (OP-EM) algorithm is given by

$$f_j^{m+1} = \frac{f_j^m}{T\sum_{i=1}^{I} p_{ij}} \sum_{i=1}^{I} p_{ij} \frac{n_i}{\sum_{b=1}^{J} p_{ib} f_b^m + \overline{\mathcal{R}}_i + \overline{\mathcal{S}}_i} \qquad (1)$$

where n_i refers to the number of events detected along LOR i (i=1...I), $\overline{\mathcal{R}}_i$ and $\overline{\mathcal{S}}_i$ denote the estimated random and scatter count rates expected along the LOR i, and T represents the scan duration.

We first divide a given scan (of duration T) into Q motion-intervals (t=1...Q) each with a duration ΔT_t within which movements remain below a given threshold. Following our notation in [11], we then introduce an invertible operator $\mathcal{L}_t()$ which models the motion of the object by transforming the LOR i along which an event *would* have been detected in the absence of motion, to the LOR i' along which the event *is* detected during interval t (Fig. 2). Motion-compensated sinograms are then obtained by binning each detected LOR i' along i=$\mathcal{L}_t^{-1}(i')$.

Next, referring to Fig. 2, we note that the time-varying (due to motion) probability $\mathcal{P}_{i'j}^t$ of detecting an event generated during interval t from voxel j along LOR i' (i.e. prior to motion correction; thus binned along LOR i following motion correction) is given by

$$\mathcal{P}_{i'j}^t = g_{ij} A_i N_{i'} \delta_{i'} \qquad (2)$$

wherein the system matrix has been decomposed into geometric g_{ij}, as well as attenuation A_i and normalization $N_{i'}$ factors, and

$$\delta_{i'} = \begin{cases} 1 & \text{if LOR } i' \text{ corresponds to a detector pair} \\ 0 & \text{otherwise} \end{cases} \qquad (3)$$

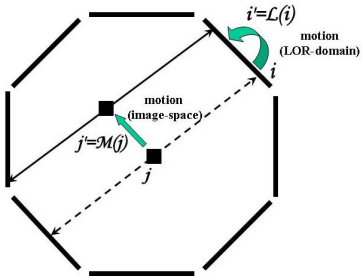

Fig. 2. An event that would have been detected along LOR i is detected along LOR i'=$\mathcal{L}\{i\}$ due to motion. In image-space, the effect of motion can be characterized by a transformation from voxel j to j=$\mathcal{M}\{j\}$.

is used to denote whether or not the LOR i' corresponds to physical detector-pairs.

In writing Eq. (2) we have noted that the normalization factor for an LOR i' along which an event is detected is given by the value of $N_{i'}$ for the LOR itself, whereas this is *not* the case for attenuation correction, due to motion of the object relative to its initial position: the attenuation factor at time t along an LOR i' is given by the measured attenuation factor at t=0 along LOR i (note that the reference time t=0 is thus taken to be the time of the transmission scan in order to correct for mis-alignments taking place between this time and the beginning of the emission scan).

We next note that the *overall* probability p_{ij} of detecting an event generated at voxel j *anytime* during the scan (t=1...T) and binned along an LOR i (after motion correction) can be written as

$$p_{ij} = \sum_{t=1}^{Q} \mathcal{P}_{i'j}^t \frac{\Delta T_t}{T} \quad \text{with} \quad i' = \mathcal{L}_t(i) \qquad (4)$$

Combining Eqs. (2) and (4), the overall system matrix can be written as:

$$p_{ij} = g_{ij} A_i \sum_{t=1}^{Q} N_{i'} \delta_{i'} \frac{\Delta T_t}{T} \quad \text{with} \quad i' = \mathcal{L}_t(i) \qquad (5)$$

Next, we define

$$\overline{N}_i = \sum_{t=1}^{Q} N_{i'} \delta_{i'} \frac{\Delta T_t}{T} \quad \text{with} \quad i' = \mathcal{L}_t(i) \qquad (6)$$

which can be thought of as the time-averaged detection-efficiency of the LORs that contribute to an LOR i upon motion correction, and using the substitution of (5) into (1), we arrive at

$$f_j^{m+1} = \frac{f_j^m}{T\overline{s}_j} \sum_{i=1}^{I} g_{ij} \frac{n_i}{\sum_{b=1}^{J} g_{ib} f_b^m + \frac{\overline{\mathcal{R}}_i}{A_i \overline{N}_i} + \frac{\overline{\mathcal{S}}_i}{A_i \overline{N}_i}} \qquad (7)$$

where

$$\overline{s}_j = \sum_{i=1}^{I} g_{ij} A_i \sum_{t=1}^{Q} N_{i'} \delta_{i'} \frac{\Delta T_t}{T} = \sum_{i=1}^{I} g_{ij} A_i \overline{N}_i \qquad (8)$$

B. Calculation of Sensitivity Factors

A number of possible (though not necessarily accurate) methods may be considered in order to simplify the computational complexity of expressions (6) or (8):

(i) By increasing the motion threshold, movements below which are neglected; thus resulting in fewer motion frames. However, this approach is bound to introduce resolution degradation and is therefore not optimal.

(ii) By application of the compression method in [10] in which neighboring LORs are grouped together. Similarly, this method is an approximation and can potentially result in inaccuracies.

(iii) Via backprojection (in Eq. 8) of only a randomized subset of the projection-space as proposed by Carson *et al.* [15]. Qi and Huesman [16] have shown that the particular randomization method is very critical in the accuracy of the estimated sensitivity factors, especially as inaccuracies will be amplified in subsequent iterations of the EM algorithm, and more accurate (yet more time-consuming) Monte Carlo randomization techniques have been proposed and are under development [17].

Our proposed approach: Alternatively, we are able to show [11] that an accurate, non-randomized *and* considerably fast method is possible. This is obtained by first noting that instead of modeling motion in the LOR-domain using the operator $\mathcal{L}_t()$, one can instead map the trajectory of the *image voxels* using an operator $\mathcal{M}_t()$ such that j'=$\mathcal{M}_t(j)$ represents the position of a voxel j during interval t, as depicted in Fig. 2.

$$g_{ij} = g_{i'j'} \quad \text{with} \quad i' = \mathcal{L}_t(i), j' = \mathcal{M}_t(j) \tag{9}$$

Next we note that if we perform attenuation *pre-correction* of the sinogram bins, the algorithm (7) is instead written as

$$f_j^{m+1} = \frac{f_j^m}{T\overline{s}_j} \sum_{i=1}^{I} g_{ij} \frac{n_i/A_i}{\sum_{b=1}^{J} g_{ib} f_b^m + \frac{\overline{\mathcal{R}}_i}{A_i \overline{N}_i} + \frac{\overline{\mathcal{S}}_i}{A_i \overline{N}_i}} \tag{10}$$

where the sensitivity term is given by

$$\overline{s}_j = \sum_{i=1}^{I} g_{ij} \sum_{t=1}^{Q} N_{i'} \delta_{i'} \frac{\Delta T_t}{T} \quad \text{with} \quad i' = \mathcal{L}_t(i) \tag{11}$$

It can then be shown [11] that

$$\overline{s}_j = \sum_{t=1}^{Q} s_{j'} \frac{\Delta T_t}{T} \quad \text{with} \quad j' = \mathcal{M}_t(j) \tag{12}$$

where s_j is the conventional sensitivity correction factor. The important result is that for any voxel j, the term $\overline{s}_j$ may be evaluated by motion-interval weighting of values of conventional sensitivity factors evaluated at j'=$\mathcal{M}_t(j)$ where j'=$j'(t)$ is the trajectory of a voxel j as it undergoes motion. In other words, the time-consuming motion-averaging in the *projection-space* (Eq. 11) can instead be performed in the *image-space*. This idea is illustrated in Fig. 3.

As an example, for a typical HRRT-scanner acquisition (span 3, maximum ring difference 67), the proposed image-space (vs. projection-space) accurate approach to the calculation of sensitivity factors can result in a factor of ∼30 speed-up in this task (the sinogram-size for a single frame is ∼470M, compared to only ∼14M voxels in image-space).

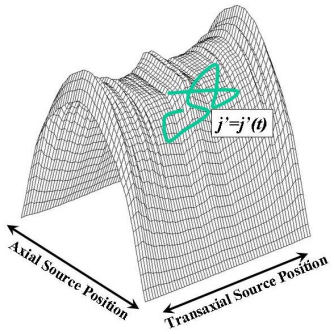

Fig. 3. The motion-compensated overall sensitivity correction factor $\overline{s}_j$ for a particular voxel j can be calculated in *image-space* by $\frac{\Delta T_t}{T}$-weighted evaluation of the conventional sensitivity term along the trajectory j'=$j'(t)$ of the voxel as measured by the tracking device (in accordance with Eq. 12).

C. Calculation of the Scatter Term

We next observe that the term $\overline{\mathcal{S}}_i/\overline{N}_i$ in (10) can also be simplified. In this work, we have used the Watson Single Scatter Simulation (SSS) technique [18]. The method has the property that instead of calculating the expected rate of scattered events S_i *detected* along each LOR i, it first calculates $\widetilde{S}_i$ *defined* such that it is related to S_i via the expression

$$S_i = \widetilde{S}_i \times N_i \tag{13}$$

wherein $\widetilde{S}_i$ is thus effectively the expected rate of *incident* scattered events.As noted by Watson [18], calculation of $\widetilde{S}_i$=S_i/N_i involves *ratios* of detector efficiencies, which can be estimated more accurately than the efficiencies themselves.

We shall argue in this section that the term $\overline{\mathcal{S}}_i/\overline{N}_i$ in (10) can be replaced by $\widetilde{S}_i$. Let us first consider the case without motion. As shown in Fig. 4, for a coincidence event detected at detectors A and B (defining an LOR i) the expected rate of scattered events S_i is given by an integral over the scattering volume V_X; i.e. for all positions X (i) at which Compton scattering could have occurred, and (ii) leading to coincidence detection by detectors A and B. For the case when the scattered event is detected at B, the integral can be written as [18]:

$$S_i = \int_{V_X} dX \, (\epsilon_{AX} \hat{\epsilon}_{BX}) \left(\frac{\sigma_{AX} \sigma_{BX}}{4\pi^2 R_{AX}^2 R_{BX}^2} \right) C_{i,X}^S(\mu, f) \tag{14}$$

where ϵ_{AX} and $\hat{\epsilon}_{BX}$ denote crystal efficiencies for events incident along AX and BX (hatted $\hat{\epsilon}$ indicates detector efficiency at the scattered photon's energy), σ_{AX} and σ_{BX} are the detector geometric cross-sections (while the distances from the scattering point X to detectors A and B are denoted by R_{AX} and R_{AX}, respectively), and finally $C_{i,X}^S(\mu, f)$ is used to denote (aside from detection efficiency considerations modeled in the previous two bracketed terms) the expected rate of events generated along the path defined by AXB and contains terms

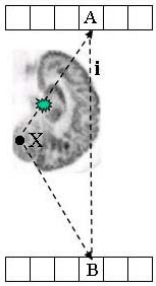

Fig. 4. A depiction of the effect of scattering at a position X resulting in a scattered event i detected along detectors A and B.

related to the distribution of density μ and activity f in the object as well as Compton scattering probabilities.

Next, noting that the normalization term N_i for the non-scattered true events detected along LOR i (corresponding to detectors A and B) has the relation [18]:

$$N_i = \frac{\epsilon_{AB}^2 \sigma_{AB}^2}{4\pi^2 R_{AB}^2} \tag{15}$$

where ϵ_{AB}^2 and σ_{AB}^2 represent the detector efficiencies and geometric cross-sections, respectively, for a non-scattered event detected along AB (with R_{AB} denoting the separation of the detectors). Defining

$$N_{i,X}^S = \frac{\epsilon_{AX}\hat{\epsilon}_{BX}\sigma_{AX}\sigma_{BX}}{4\pi^2 R_{AX}^2 R_{BX}^2} \tag{16}$$

as the corresponding overall efficiency for detection of scattered events along LOR i (scattered at X), then referring to (14) it is easy to see that the term $\widetilde{S}_i$ in (13) can be written as:

$$\widetilde{S}_i = \int_{V_X} dX \frac{N_{i,X}^S}{N_i} C_{i,X}^S(\mu, f) \tag{17}$$

Effect of motion: Similar to true coincidences, each scattered event detected at time t and binned (after motion correction) along an LOR i was initially detected along an LOR i'=$\mathcal{L}_t(i)$. Then, defining $S_{i'}^{det}(t)$ as the expected rate of scattered events *detected* along LOR i' at time interval t (therefore binned along LOR i), we note that $\overline{\mathcal{S}}_i$ in (10), which represents the overall rate of detected scattered events (i.e. over the *entire* duration of the scan) binned along LOR i, can be expressed as:

$$\overline{\mathcal{S}}_i = \sum_{t=1}^{Q} S_{i'}^{det}(t) \frac{\Delta T_t}{T} \quad \text{with} \quad i' = \mathcal{L}_t(i) \tag{18}$$

Next, similar to the definition of $\widetilde{S}_i$ in the expression (13), we define $S_{i'}^{inc}(t)$ such that:

$$S_{i'}^{det}(t) = S_{i'}^{inc}(t) \times N_{i'}\delta_{i'} \tag{19}$$

wherein $S_{i'}^{inc}(t)$ is thus effectively the expected rate of scattered events *incident* along LOR i' at time interval t, and wherein using $\delta_{i'}$ we have taken into consideration the fact that $S_{i'}^{det}(t)$ will be zero if i' now exits the FoV (e.g. when motion causes the LOR to exit the scanner axially). Subsequently, similar to Eq. (17), $S_{i'}^{inc}(t)$ can be expressed as:

$$S_{i'}^{inc}(t) = \int_{V_X} dX \frac{N_{i',X'}^S}{N_{i'}} C_{i',X'}^S(\mu', f') \tag{20}$$

where the primed quantities indicate the effect of motion transformation of the scattering volume at time interval t.

At this stage, we shall argue that expression (20) for $S_{i'}^{inc}(t)$ (where i'=$\mathcal{L}_t(i)$) is nearly equivalent to the conventionally computed scatter term $\widetilde{S}_i$ as given by (17). To proceed, we will assume the following:

(1) The motion operator $\mathcal{L}_t()$ applied to true-coincidence LORs is similarly applicable to modeling the motion of scattered-event LORs. This assumption is not strictly true [19] for a large translation, in cases when motion results in significant change in the relation between the object and the scanner. In this work, however, given realistic amounts of motion, and the smooth nature of the scattering distribution, we shall assume that this is the case, and that therefore, the relation of i' with respect to the attenuation μ' and emission f' distributions remains nearly the same, and therefore

$$C_{i',X'}^S(\mu', f') \approx C_{i,X}^S(\mu, f) \tag{21}$$

(2) While the absolute efficiency of detection $N_{i',X'}^S$ (consisting of intrinsic and geometric factors) certainly varies with motion and is taken into account in this work, the *relative* detection efficiencies between the scattered and true events are nearly preserved with motion; i.e.

$$\frac{N_{i',X'}^S}{N_{i'}} \approx \frac{N_{i,X}^S}{N_i} \tag{22}$$

In addition, this is effectively true particularly given the wide-range of angles/positions from which scattered events contribute to an LOR.

Combining Eqs. (17), (20), (21) and (22), one arrives at the intuitively appealing result:

$$S_{i'}^{inc}(t) \approx \widetilde{S}_i \quad \text{with} \quad i' = \mathcal{L}_t(i) \tag{23}$$

where $\widetilde{S}_i$, in this work, is obtained using the standard Watson single scatter simulation (SSS) method [18] (on motion corrected sinograms). Combining Eqs. (18), (19) and (23), it then follows that

$$\overline{\mathcal{S}}_i \approx \sum_{t=1}^{Q} \left[\widetilde{S}_i \times N_{i'}\delta_{i'} \frac{\Delta T_t}{T} \right] = \widetilde{S}_i \overline{N}_i \tag{24}$$

where we have used the definition (6) for $\overline{N}_i$. This gives a very intuitive picture: the overall rate $\overline{\mathcal{S}}_i$ of detected scattered events binned (after motion correction) along an LOR i is given by the rate $\widetilde{S}_i$ of such events normally *incident* (i.e. in the absence of any motion) along the LOR, multiplied by the motion-weighted normalization factor $\overline{N}_i$. As a result, the expression $\overline{\mathcal{S}}_i/\overline{N}_i$ in (10) can be simply replaced by the regularly calculated expression $\widetilde{S}_i$.

D. Calculation of the Random Term

We begin by noting that, similar to Eq. (18), the overall expected rate $\overline{\mathcal{R}}_i$ of random coincidences binned along LOR i can be written as

$$\overline{\mathcal{R}}_i = \sum_{t=1}^{Q} R_{i'}^{det}(t)\frac{\Delta T_t}{T} \quad \text{with} \quad i' = \mathcal{L}_t(i) \tag{25}$$

where $R_{i'}^{det}(t)$ denotes the expected rate of random events detected along LOR i'=$\mathcal{L}_t(i)$ at time interval t (therefore binned along LOR i).

Next, we note that ordinarily, unlike analytic calculations for expected scatter counts, the expected random counts are more directly obtained (from singles or delayed-coincidences). As such, the term $\overline{\mathcal{R}}_i$ can be directly computed using one of these two general approaches (i.e. from motion corrected singles or delayed coincidences). As a result, the expression $\overline{\mathcal{R}}_i/\overline{N}_i$ in (10) can in principle be calculated. However, (i) the task of computing $\overline{N}_i$ remains a computationally intense one (which, for instance, in the case of the sensitivity term was avoided as discussed in Sec. III-B), and (ii) motion compensated binning of delayed coincidences, and especially singles counts (which arrive from different orientations), may not be feasible. As such, we have pursued an alternative, more practical approach, as described next.

Similar to Eq. (19), we define $R_{i'}^{inc}(t)$ such that

$$R_{i'}^{det}(t) = R_{i'}^{inc}(t) \times N_{i'}\delta_{i'} \tag{26}$$

wherein $R_{i'}^{inc}(t)$ effectively denotes the rate of random events incident along an LOR i' at time interval t.

At this stage, we make the following simplifying approximation: due to the very broad nature of random contributions compared to realistic amounts of motion, we assume that motion does not alter the rate of randoms *incident* along an LOR (i.e. $R_i^{inc}(t)$ is a constant in time), and that incident randoms along any LOR i and its motion-transformed LOR i'=$\mathcal{L}_t(i)$ are nearly the same (i.e. $R_i^{inc}(t)$≈$R_{i'}^{inc}(t)$). We summarize this by writing:

$$\widetilde{R}_i \equiv R_i^{inc}(t) \approx R_{i'}^{inc}(t) \quad \text{with} \quad i' = \mathcal{L}_t(i) \tag{27}$$

wherein $\widetilde{R}_i$ is introduced to emphasize time/motion-independence of $R_i^{inc}(t)$. One can then write:

$$R_i^{det}(t) \approx \widetilde{R}_i \times N_i\delta_i \tag{28}$$

from which we similarly concluded that R_i^{det}=$R_i^{det}(t)$ is nearly a constant in time, and is simply given by the overall mean rate of random coincidences detected along any LOR i, as ordinarily computed in PET imaging applications.

Furthermore, combining Eqs. (25), (26) and (27), one arrives at:

$$\overline{\mathcal{R}}_i \approx \sum_{t=1}^{Q}\left[\widetilde{R}_i \times N_{i'}\delta_{i'}\frac{\Delta T_t}{T}\right] = \widetilde{R}_i\overline{N}_i \tag{29}$$

It then follows that, considering the above two equations, for LORs within the FoV (i.e. δ_i=1):

$$\widetilde{R}_i \approx \frac{\overline{\mathcal{R}}_i}{\overline{N}_i} \approx \frac{R_i^{det}}{N_i} \quad \text{for} \quad \delta_i = 1 \tag{30}$$

In other words, for binned LORs i that are inside the FoV (δ_i≠0), the expression $\overline{\mathcal{R}}_i/\overline{N}_i$ in the overall EM algorithm (Eq. 10) may be replaced with R_i^{det}/N_i.

Nevertheless, for motion-compensated events that are outside the FoV (i.e. δ_i=0), it is not possible to extract the incident random rates $\widetilde{R}_i$ (and therefore $\overline{\mathcal{R}}_i/\overline{N}_i$) from (28). As such, for these LORs, given the broad nature of the randoms distribution, we have used the values obtained by extrapolating to nearby LORs in the FoV, which we shall refer to as $extrap\left\{\frac{R_i^{det}}{N_i}\right\}$. Thus, re-defining

$$\widetilde{R}_i \equiv \begin{cases} \frac{R_i^{det}}{N_i} & \delta_i = 1 \\ extrap\left\{\frac{R_i^{det}}{N_i}\right\} & \delta_i = 0 \end{cases} \tag{31}$$

in relation to Eq. (30), we finally arrive at the estimation

$$\frac{\overline{\mathcal{R}}_i}{\overline{N}_i} \approx \widetilde{R}_i \quad \text{for all } i \tag{32}$$

Subsequently, we may replace the expression $\overline{\mathcal{R}}_i/\overline{N}_i$ in (10) by $\widetilde{R}_i$, where $\widetilde{R}_i$ is given by (31).

Final Result: Combining results of Secs. III-B, III-C and III-D, as given by Eqs. (12), (24) and (32), respectively, the motion-compensated EM algorithm (10) can be written in the final form:

$$f_j^{m+1} = \frac{f_j^m}{T\sum_{t=1}^{Q} s_{j'}\frac{\Delta T_t}{T}}\sum_{i=1}^{I} p_{ij}\frac{n_i/A_i}{\sum_{b=1}^{J} p_{ib}f_b^m + \frac{\widetilde{R}_i}{A_i} + \frac{\widetilde{S}_i}{A_i}} \tag{33}$$

wherein $s_{j'}$ is the conventional sensitivity term evaluated at the motion-trajectory j'=$\mathcal{M}_t(j)$ (see Fig. 3), $\widetilde{S}_i$ is the standard scatter estimate obtained using the single scatter simulation (SSS) method (on motion corrected sinograms), and $\widetilde{R}_i$ is given by (31).

E. List-mode Image Reconstruction

The list-mode approach has the inherent advantage of *naturally* incorporating all detected events, avoiding the burden of extending the sinogram-space in histogram-mode methods (in order to include motion-compensated, binned events that are out of the FoV). We have elaborated the derivation of the motion-compensated list-mode EM algorithm elsewhere (Appendix I of [11]).

In the present work, we also include time/motion-varying random and scatter terms in the list-mode algorithm. Denoting l_k as the LOR along which the kth list-mode event is detected (k=1...K) and i_k=$\mathcal{L}_t^{-1}(l_k)$ as the corresponding motion-corrected LOR, the algorithm can be written as

$$f_j^{m+1} = \frac{f_j^m}{T\bar{s}_j}\sum_{k=1}^{K} g_{i_k j} \times \frac{1/A_i}{\sum_{b=1}^{J} g_{i_k b}f_b^m + \frac{R_l^{det}(t)}{A_i N_l} + \frac{S_l^{det}(t)}{A_i N_l}} \tag{34}$$

where the sensitivity term $\bar{s}_j$ is given by Eq. (12), and $R_l^{det}(t)$ and $S_l^{det}(t)$ (Secs. III-C and III-D) are the mean randoms and scattered coincidence events detected along an LOR l during interval t.

F. Scatter/Random Corrections in List-mode Reconstruction

Similar to the term $\overline{\mathcal{S}}_i/\overline{N}_i$ in the histogram-mode algorithm (10), the term $S_l^{det}(t)/N_l$ in the above list-mode algorithm (34) can also be seen to essentially estimate the expected rates of scatter coincidences *incident* along an LOR l at time t (therefore, along LOR i=$\mathcal{L}_t^{-1}(l)$ following motion correction). More rigorously, for a detected LOR l (i.e. prior to motion correction; thus δ_l=1 necessarily), one may combine Eqs. (19), (23) and (24), to arrive at

$$\frac{S_l^{det}(t)}{N_l} \approx \frac{\overline{\mathcal{S}}_i}{\overline{N}_i} \approx \widetilde{S}_i \quad \text{with} \quad i = \mathcal{L}_t^{-1}(l) \tag{35}$$

Within the framework of Sec. III-D, a very similar relation exists for random coincidences; combining Eq. (26), (27) and (29), one arrives at:

$$\frac{R_l^{det}(t)}{N_l} \approx \frac{\overline{\mathcal{R}}_i}{\overline{N}_i} \approx \widetilde{R}_i \quad \text{with} \quad i = \mathcal{L}_t^{-1}(l) \tag{36}$$

wherein $R_l^{det}(t)/N_l$ and $\overline{\mathcal{R}}_i/\overline{N}_i$ both estimate the average rate of random events *incident* along an LOR l (therefore along i=$\mathcal{L}_t^{-1}(l)$ following motion correction). Using the aforementioned two relations, algorithm (34) can be written in the final form:

$$f_j^{m+1} = \frac{f_j^m}{T\sum_{t=1}^{Q} s_{j'}\frac{\Delta T_t}{T}} \sum_{k=1}^{K} \frac{g_{i_k j} \quad 1/A_i}{\sum_{b=1}^{J} g_{i_k b} f_b^m + \frac{\widetilde{R}_i}{A_i} + \frac{\widetilde{S}_i}{A_i}} \tag{37}$$

wherein, similarly to the histogram-mode counterpart (33), $s_{j'}$ is the conventional sensitivity term evaluated at the motion-trajectory j'=$\mathcal{M}_t(j)$ (Fig. 3), $\widetilde{S}_i$ is the standard scatter estimate obtained using the single scatter simulation (SSS) method (on motion corrected data), and $\widetilde{R}_i$ is given by (31).

IV. Methods

Tomograph: Data were acquired on the second generation high resolution research tomograph (HRRT) [22].

Motion-Tracking: Collection of motion data was carried out using a Polaris motion tracking system. This system uses an infrared signal to track a small tool consisting of four retro-reflective spheres attached to a plastic plate. Each motion measurement (quaternion and translation) was output in binary format with a time stamp that was synchronized to the HRRT acquisition PC using a common time server.

Phantom Study: An elaborate motion study was performed involving a number of distinct movements (as summarized in table I) on an elliptical contrast phantom (3.2L) containing hot (31mL) and cold (13mL) spheres inserted in a background. The phantom was filled with a total F-18 activity of 1.047 mCi (resulting in initial prompts and randoms rates of 267 kcps and 27 kcps), while the hot/background ratio was 4.77.

Mathematical brain phantom: A new mathematical brain phantom was developed, containing continuous structures and thus avoiding the need for interpolations when introducing motion, as depicted in Fig. (5). The brain phantom was constructed using subdivision surfaces [23]. Surfaces were modeled based on a segmented MRI dataset of a normal subject. The dataset consisted of 181 slices of the brain (pixel-sizes/slice-widths of 1.0 mm's). One-hundred structures in the brain were identified.

TABLE I

Table of Phantom Movements (with respect to time=0)

Frame	Time (min)	x-axis	y-axis	z-axis
1	0 - 2	0	0	0
2	2 - 4	0	+5°	0
3	4 - 6	0	-5°	0
4	6 - 8	0	0	+3°
5	8 - 10	0	0	+6°
6	10 - 12	0	0	+9°
7	12 - 14	+5°	0	0
8	14 - 16	+15°	0	0
9	16 - 18	0	0	+10 mm
10	18 - 20	0	+10 mm	+10 mm
11	20 - 22	0	+10 mm	+20 mm
12	22 - 24	0	+20 mm	+20 mm
13	24 - 26	0	+20 mm	+30 mm
14	26 - 28	0	+30 mm	+30 mm

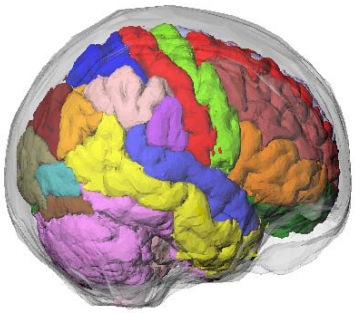

Fig. 5. New Mathematical Brain Phantom.

PET Simulations: A new simulation technique [24] was used involving combination of two powerful and well-validated Monte-Carlo codes, SimSET and GATE. The method takes advantage of the shorter simulation times for photon propagation inside a digital phantom using SimSET as compared to GATE. We used the design parameters and the geometry of the second generation HRRT scanner.

In this work, movement of the patient in-between three positions were simulated, each moved with respect to one another by 4.6 mm, 4.6 mm and 7.0 mm in the x (horizontal), y (vertical), and z (axial) directions, respectively, consistent with actually observed amounts of motion. Simulations involving 32M, 77M and 209M detected events were considered.

Reconstructions: Experimental/simulated data for the HRRT were reconstructed directly from the list-mode data (see [21] for details) with spans of 3/9, a maximum ring difference of 67, and using 32 subsets. Four reconstruction scenarios were considered: (i) No motion (with matched statistics), (ii) motion with no compensation, (iii) purely LOR-driven compensation, and (iv) the proposed accurate motion-compensation algorithm (37).

Quantitative Metrics: For the phantom study, hot and cold contrast were estimated following approximately the NEMA NU 2001 protocol. Defining C_H, C_C and C_B as average measured counts in regions of interest (ROIs) placed in hot, cold and background regions, respectively, the cold percent contrast Q_C was measured using $Q_C = \left(1 - \frac{C_C}{C_B}\right) \times 100\%$ while the hot percent contrast Q_H was calculated using $Q_H = \frac{C_H/C_B - 1}{A_H/A_B - 1} \times 100$ where A_H/A_B is the actual concentration ratio between the hot and background regions (measured to be 4.77). The percent noise (standard deviation/mean$\times$100%) was calculated for a large background ROI.

For the simulations, different areas in the brain (caudate, putamen, grey, white, cerebellum and brain stem) were quantitatively analyzed. NSD values for each region (r=1...R where R=6) were calculated by:

$$\text{NSD}_r = \frac{\sqrt{\frac{1}{n-1}\sum_{j \in r}(\lambda_j - \bar{\lambda}^r)^2}}{\bar{\lambda}^r} \tag{38}$$

where λ_j denotes the reconstructed value at voxel j, $\bar{\lambda}^r$ is the average value over each region r, and n is the number of voxels $j \in r$ defining ROI r. The overall bias was also measured using an ROI-based normalized mean squared error (NMSE) metric given by:

$$\text{NMSE} = \frac{1}{R}\sum_{r=1}^{R}\left(\frac{\bar{\lambda}^r - \mu^r}{\mu^r}\right)^2 \tag{39}$$

where μ^r denotes the activities used as (true) reference in each ROI as obtained using 20 iterations of a static, high-statistic (300M events) simulation of the same brain phantom.

V. Results and Discussion

Phantom Study: Fig. (6) shows typical transaxial and coronal slices for reconstructions of the entire phantom study (i.e. including all frames 1-14 in table I) for cases of (i) no motion correction, (ii) purely LOR-driven correction, and (iii) the proposed method. Unlike the proposed approach, very strong artifacts are observed for the conventional motion correction scheme (highly resembling patterns seen in a sensitivity image for the HRRT scanner, explained by the fact that the conventional scheme does not take into account sensitivity variations for individual voxels as they move in the FoV).

For a quantitative comparison, Figs. (7a,b) show plots of cold Q_C and hot Q_H percent contrasts vs. percent noise for frame 1 (reference) as well as motion frames 3, 8, 10 and 12 (see table I). In line with frame 1, it is clearly seen that plots obtained using the proposed (- -) motion correction method outperform those by the conventional (dotted) purely event-driven motion correction method.

Simulations: Figure 8 depicts typical transaxial and coronal slices for reconstructions in the cases of (i) no motion, (ii) motion with no compensation, (iii) purely LOR-driven correction, and (iv) the proposed method, for 209M simulated events. It is clearly observed that purely LOR-driven corrections lead to considerable artifacts (similar results were obtained for 32M and 77M events).

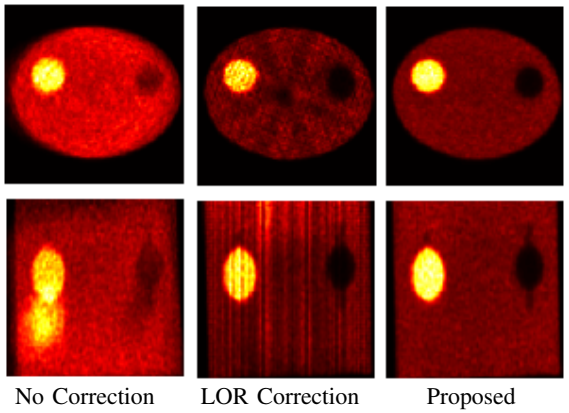

Fig. 6. Reconstructed images after 2 iterations (32 subsets); (column 1) No Motion Correction (MC), (column 2) Purely LOR-driven MC, (column 3) proposed MC. Transaxial and coronal slices are shown in the first and second rows, respectively.

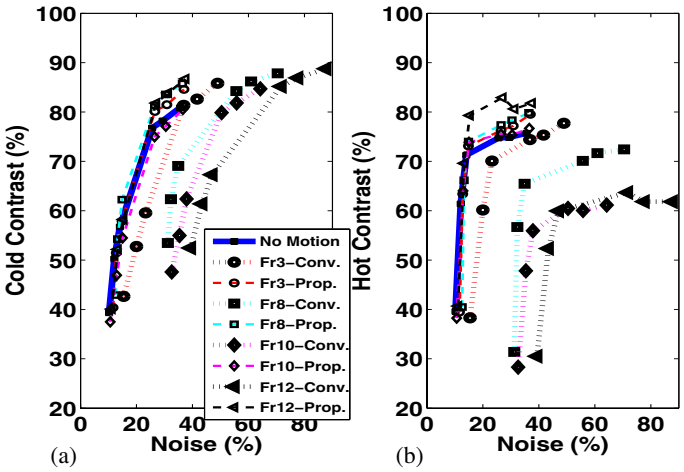

(a) (b)

Fig. 7. Plots of (a) cold percent contrast Q_C and (b) hot percent contrast Q_H (vs. percent noise) for frame 1 (reference) as well as frames 3, 8, 10 and 12 (table I) for conventional (dotted) and proposed (- -) event-driven schemes.

To study the proposed approach quantitatively, Fig. 9 shows plots of NSD (noise) vs. NMSE (bias), as defined in the previous section, for two different statistics. It is similarly observed that the proposed scheme poses an improvement relative to the purely LOR-driven approach, and is very comparable with simulations involving no motion (and with matched statistics).

VI. Conclusion

We have proposed and investigated a formalism for accurate motion-compensated EM reconstruction, including elaborate consideration of randoms and scattered events, which is particularly feasible in the context of high-resolution PET. The method takes into consideration presence of motion-induced interactions between lines-of-response (LORs) within and outside the field-of-view (FoV), and accurately incorporates *all* detected events, including those, for instance, which exit the scanner axially or pass through detector gaps following motion correction. As an example, for a typical HRRT-scanner acquisition, the proposed *image-space* (vs. projection-space) accurate

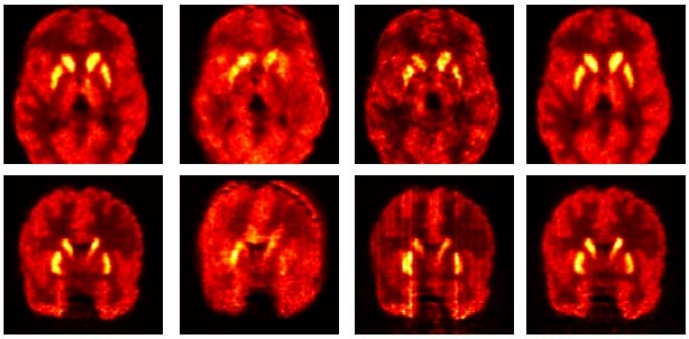

Fig. 8. Simulation contained 209M detected events. Reconstructed images after 2 iterations (32 subsets); (column 1) No motion, (column 2) No Motion Correction (MC), (column 3) Purely LOR-driven MC, (column 4) proposed MC. Transaxial and coronal slices are shown in the first and second rows, respectively.

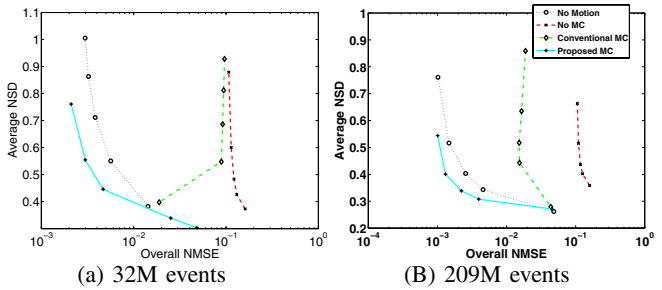

(a) 32M events (B) 209M events

Fig. 9. Plots of NSD (noise) vs. NMSE (bias) with increasing iterations for different simulations. The proposed method outperforms the purely LOR-driven approach.

calculation of the sensitivity factors can result in a factor of $\sim$30 speed-up in this task.

The method has been furthermore extensively tested using experimental as well as simulation studies involving a new mathematical brain phantom and a novel combination of SimSET and GATE simulation packages. It has been demonstrated that, in comparison to reconstructions of data with matched statistics involving no motion, the proposed method removes qualitative artifacts as well as quantitative inferiorities of purely event-driven correction methods.

ACKNOWLEDGMENTS

This work was supported by the National Institute of Health, the TRIUMF Life Science Grant, the Natural Sciences and Engineering Research Council of Canada, and the Michael Smith Foundation for Health Research. The authors wish to especially thank Andrew Crabb, Kelvin Raywood and Ken Buckley for computational and technical support.

REFERENCES

[1] R. R. Fulton, S. R. Meikle, S. Eberl, J. Pfeiffer, and C. J. Constable, "Correction for head movement in positron emission tomography using an optical motion tracking system", *IEEE Trans. Nucl. Sci.*, vol. 49, pp. 116-123, 2002.

[2] Y. Picard, and C. J. Thompson, "Motion correction of PET images using multiple acquisition frames", *IEEE Trans. Med. Imag.*, vol. 16, pp. 137-144, 1997.

[3] M. Menke, M. S. Atkins, and K. R. Buckley, "Compensation Methods for Head Motion Detected During PET Imaging", *IEEE Trans. Nucl. Sci.*, vol. 43(1), pp. 310-317, 1996.

[4] R. R. Fulton and S. R. Meikle, "Reconstruction of Projection Data Corrupted by Rigid or Non-Rigid Motion", oral presentation at *IEEE Med. Imag. Conf*, 2005.

[5] M. Reyes, G. Malandain, P. M. Koulibaly, and J. Darcourt, "Respiratory Motion Correction in Emission Tomography Imaging" *Proceed. 8th Intern. Meeting. Fully 3D Image Recon. Radiol. Nucl. Med.*, pp. 110-113, 2005.

[6] F. Qiao, T. Pan, J. W. Clark, O. R. Mawlawi, "Motion-Incorporated Reconstruction Method for Gated PET Studies", *Phys. Med. Biol.*, pp. 3769-3783, 2006.

[7] T. Li, B. Thorndyke, E. Schreibmann, Y. Yang, and L. Xing, "Model-based image reconstruction for four-dimensional PET" *Med. Phys. Vol.*, vol. 33, pp. 1288-1298, 2006.

[8] A. Rahmim, J. C. Cheng, K. Dinelle, M. Shilov, W. P. Segars, O. G. Rousset, B. M. W. Tsui, D. F. Wong, V. Sossi "System Matrix Motion Modeling of Externally Tracked Motion", *IEEE Med. Imag. Conf.*, 2006.

[9] M. E. Daube-Witherspoon, Y. C. Yan, M. V. Green, R. E. Carson, K. M. Kempner, and P. Herscovitch, "Correction for motion distortion in PET by dynamic monitoring of patient position (Abstract)", *J. Nucl. Med.*, vol. 31, pp. 816, 1990.

[10] P. Bühler, U. Just, E. Will, J. Kotzerke, and J. van den Hoff, "An Accurate Method for Correction of Head Movement in PET.", *IEEE Trans. Med. Imag.*, vol. 23(8), pp. 1176-1185, 2004.

[11] A. Rahmim, P. Bloomfield, S. Houle, M. Lenox, C. Michel, K. R. Buckley, T. J. Ruth, and V. Sossi, "Motion compensation in histogram-mode and list-mode EM reconstructions: beyond the event-driven approach", *IEEE Trans. Nucl. Sci.*, vol. 51, pp. pp. 2588-2596 (2004).

[12] J. Qi and R. H. Huesman, "Correction of Motion in PET using Event-Based Rebinning Method: Pitfall and Solution (Abstract)", *J. Nucl. Med.*, vol. 43, pp. 146P, 2002.

[13] J. Qi and R. H. Huesman, "List mode reconstruction for PET with motion compensation: a simulation study", *Proc. IEEE Inter. Symp. Bio. Imag.*, pp. 413-416, 2002.

[14] K. Thielemans, S. Mustafovic, and L. Schnorr, "Image Reconstruction of Motion Corrected Sinograms", *IEEE NSS/MIC Conf. Record*, vol. 4, pp. 2401-2406, 2003.

[15] R. E. Carson, W. C. Barker, J. S. Liow, and C. A. Johnson, "Design of a motion-compensation OSEM list-mode algorithm for resolution-recovery reconstruction for the HRRT", *IEEE NSS/MIC. Conf. Record.*, vol. 5, pp. 3281-3285, 2003.

[16] J. Qi and R. H. Huesman, "Propagation of errors from the sensitivity image in list mode reconstruction", *IEEE Trans. Med. Imag.*, vol. 23, pp. 1094-1099, 2004.

[17] J. Qi, "Calculation of the Sensitivity Image in List-Mode Reconstruction", *IEEE Med. Imag. Conf.*, Oct 2005.

[18] C. C. Watson, "New, Faster, Image-Based Scatter Correction for 3D PET", *IEEE Trans. Nucl. Sci.* , vol. 47, pp. 1587-1594, 2000.

[19] K. Thielemans, "Scatter Estimation and Motion Correction in PET", *IEEE NSS/MIC. Conf. Record*, vol. 3, pp. 23-29, 2005.

[20] L. Parra and H. H. Barrett, "List-mode Likelihood: EM algorithm and image quality estimation demonstrated on 2-D PET", *IEEE Trans. Med. Imag.*, vol. 17, no. 2, pp. 228-235, 1998.

[21] A. Rahmim, J. C. Cheng, S. Blinder, M-L. Camborde, and V. Sossi, "Statistical dynamic image reconstruction in state-of-the-art high resolution PET , *Phys. Med. Biol.*, vol. 50, pp. 4887-4912, 2005.

[22] V. Sossi, H.W.A.M. de Jong, W. C. Barker, P. Bloomfield, Z. Burbar, M-L. Camborde, C. Comtat, L. A. Eriksson, S. Houle, D. Keator, C. Knob, R. Krais, A. A. Lammertsma, A. Rahmim, M. Sibomana, M. Teras, C. J. Thompson, R. Trebossen, J. Votaw, M. Walker, K. Wienhard, D. F. Wong,, "The second generation HRRT - a multi-centre scanner performance investigation", *IEEE NSS/MIC Conf. Record*, vol. 4, pp. 23-29, 2005.

[23] H. Hoppe, T. DeRose, T. Duchamp, M. Halstead, H. Jin, J. McDonald, J. Schweitzer, W. Stuetzle, "Piecewise smooth surface reconstruction", Computer Graphics, vol. 28, pp. 295-302, 1994.

[24] M. A. Shilov, E. C. Frey, W. P. Segars, J. Xu, and B. M. W. Tsui, "Improved Monte-Carlo Simulations for Dynamic PET", society of nuclear medicine publication, 2006.